Main Manuscript

HES1 oscillations are required for cell cycle re-entry in oestrogen receptor positive breast cancer cells

Oliver Cottrell[1], Andrew Rowntree[1], Benjamin Noble[1], Robert B. Clarke[2], Nancy Papalopulu[1]*

[1] Division of Developmental Biology and Medicine, School of Medical Sciences, Faculty of Biology Medicine and Health, The University of Manchester, Michael Smith Building, Oxford Road, Manchester, M13 9PL, UK

[2] Manchester Breast Centre, Division of Cancer Sciences, School of Medical Sciences, Faculty of Biology Medicine and Health, The University of Manchester, Oglesby Cancer Research Building, Wilmslow Road, Manchester, M20 4GJ, UK.

* Correspondence: nancy.papalopulu@manchester.ac.uk

Abstract

Long-term recurrence in breast cancer is driven by reactivation of dormant disseminated tumour cells (DTCs) and remains a major clinical challenge, particularly in oestrogen receptor positive (ER^+) tumours. This process is underpinned by regulation of the cell cycle machinery that controls quiescence maintenance and exit. HES1, a Notch pathway transcription factor, regulates key cell cycle genes and has been shown to demonstrate protein expression oscillations which are crucial to its function.

Here, we sought to establish whether HES1 oscillations may regulate ER+ cancer cell quiescence and reactivation. To investigate this, we developed a fundamental *in vitro* model of cell cycle arrest and re-entry based on reversible CDK4/6 inhibition (CDK4/6i), compatible with quantitative single-cell live-imaging of an endogenous HES1 reporter. Consistent with earlier findings, HES1 exhibited ~24-hour protein oscillations in cycling cells demonstrating a reproducible dip in protein expression prior to G1/S. During CDK4/6i-mediated arrest the ~24h HES1 oscillation was lost, HES1 levels were maintained at a moderately higher level and HES1 exhibited smaller dips. Similar changes were observed in unperturbed, spontaneously quiescent cells. Following release from CDK4/6i and cell cycle re-entry, these alterations were reversed and the characteristic G1/S HES1 dip was observed. Preventing this dip at the point of release, by inducibly sustaining HES1 with a Tet-On system, impeded cell cycle re-entry and induced cell death. These findings suggest that manipulating HES1 dynamics could represent a promising therapeutic approach to prevent reactivation of dormant tumour cells.

Significance Statement

Breast cancer can recur years after initial treatment due to reactivation of dormant tumour cells. Understanding how these cells exit dormancy is crucial for preventing relapse. We investigated HES1, a transcription factor with rhythmic protein oscillations, and its role in regulating quiescence in oestrogen receptor-positive (ER^+) breast cancer cells. Using live-cell imaging and a reversible cell cycle arrest model, we show that HES1 dynamics change during dormancy and reactivation, and that disrupting these oscillations prevents cell cycle re-entry and induces cell death. These findings reveal HES1 protein dynamics as a potential therapeutic vulnerability and highlight a novel strategy to target dormant cancer cells to prevent their reactivation.

Introduction

Breast cancer is the leading class of female cancer worldwide, with around 1 in 7 women now expected to develop the cancer in their lifetime (Smitenaar *et al*., 2016; Ferlay *et al*., 2018). In recent decades, mortality rates have been markedly reduced by earlier diagnosis and improved targeted therapeutic options. Despite advances in 5-year survival however, the risk of relapse, metastasis and fatality persists beyond that point. This is particularly evident in ER+ luminal breast cancers, where the rate of recurrence within 20 years ranges from 15-38%, depending on the extent of spread at diagnosis (Pan *et al*., 2017).

Indeed, long-term distant recurrence, can present up to 20 years following the termination of primary adjuvant therapy in ER+ breast cancer patients (Pan *et al*., 2017; Bushnell *et al*., 2021). This points towards long periods of clinical dormancy, where tumours remain in stasis at secondary sites, retaining the propensity to later resume growth and form overt metastases. This can occur at the level of the tumour mass, where the proliferation rate of micro-metastases is balanced by immune-surveillance and limited vascularisation, as well as at the single-cell level, where individual DTCs are functionally quiescent (Sosa *et al*., 2014; Phan and Croucher, 2020).

Recent research has significantly advanced our understanding of DTC dormancy. Rather than arising from reproducible mutations, dormancy has been associated with epigenetic reprogramming, with repressive chromatin marks shaping transcriptional programmes that sustain quiescence (Sosa et al., 2015; Rosano et al., 2024). These transcriptional programmes are not static but can be shaped or re-wired by cues from the tumour microenvironment (TME), where immune cells, stromal cells, and hypoxia have emerged as key modulators of dormancy and reactivation (Correia et al., 2021; Borriello et al., 2022; Baldominos et al., 2022; Turrell et al., 2022; Wang et al., 2023; Bushnell et al., 2024). Despite these insights, no therapeutic options for managing dormant DTCs currently exist, highlighting the urgent need

to better understand the mechanisms and pathways by which DTCs transition between dormancy and reactivation.

The Notch signalling pathway is a potent regulator of cell fate and proliferation during development across multiple tissues, including the mammary gland (Edwards et al., 2021; Chen et al., 2021). Dysregulation of Notch signalling has been implicated in tumorigenesis across various contexts (Politi *et al*., 2004; Siebel and Lendahl, 2017; Shi *et al*., 2024). Moreover, Notch signalling has been shown to be important for engraftment of dormant niches in the bone marrow by breast DTCs (Capulli *et al*., 2019), while Notch signalling is strongly upregulated in NR2F1 agonist-induced dormancy (Khalil *et al*., 2022).

Downstream of Notch signalling, HES1 a transcriptional repressor, has also been implicated in cancer. HES1 is upregulated in primary luminal A breast cancer compared to paired healthy mammary cells from the same patient (Li *et al*., 2024). Furthermore, in hormone therapy resistant ER+ breast cancer cell lines and patient-derived xenograft (PDX) tumours, HES1 is upregulated in the cancer stem cells which are likely to be the source of breast cancer recurrence (Simoes *et al*., 2015). At the molecular level**,** HES1 modulates proliferation by transcriptional repression of several elements of the cell cycle machinery, including CycD1, CycE2, CycA2, E2F, p21 and p27 (Castella *et al*., 2000; Hartman *et al*., 2004; Murata *et al*., 2005; Noda *et al*., 2011; Cenciarelli *et al*., 2017). Thus, overexpression of HES1 in an ER+ breast cancer cell line, reduced proliferation by repression of E2F-1 (Hartman *et al*., 2004), while HES1 downregulation by HES6 had the reverse effect (Hartman *et al*., 2009).

These studies have illustrated the relevance of HES1 to breast cancer with an emphasis on their mean levels of expression. However, developmental studies have indicated that Notch pathway components regulate cell fate and proliferation by virtue of their dynamic gene expression patterns. Specifically, Notch ligands (Dll1), direct Notch targets (HES1, HES5) and their downstream targets (ASCL1, NGN2, NGN3) have been shown to periodically fluctuate (i.e. oscillate) at the protein level. The characteristics of these oscillations (amplitude, frequency and phase), rather than mean expression levels alone, have been shown to functionally regulate somitic, neural and pancreas development (Shimojo *et al*., 2008; Imayoshi *et al*., 2015; Manning *et al*., 2019; Zhang *et al*., 2021; Miller *et al*., 2025).

Moreover, manipulating HES1 from wild-type oscillatory dynamics to sustained expression in adult neural stem cells (NSCs) has been shown to reduce proliferation rate (Sueda *et al*., 2019; Maeda *et al*., 2023) and prevent re-entry from cell cycle arrest (Marinopoulou *et al*., 2021), via differential regulation of p21 (Marinopoulou *et al*., 2021; Maeda *et al*., 2023).

Motivated by the functional importance of dynamics, our recent work investigated HES1 oscillations in ER+ breast cancer (Sabherwal *et al*., 2021), uncovering a cell cycle-associated periodicity of ~25h, which was similar to the average cell cycle length (~24h). An oscillatory dip in HES1 expression reliably occurred prior to S-phase, ~10-14 hours prior to the next division, leading us to hypothesise that HES1 oscillations are required for the G1/S transition.

Here, we investigate the relevance of HES1 oscillations specifically to cell cycle re-entry from quiescence. To study tumour dormancy and recurrence with multi-day quantitative single-cell live-imaging with high temporal resolution, an in vitro model of cell cycle arrest and re-entry was developed using reversible CDK4/6 inhibition (CDK4/6i) in an ER+ breast cancer cell line. We show that during arrest the cell cycle-associated HES1 oscillations are absent but are rescued upon cell cycle re-entry. Manipulating HES1 oscillations, using an inducible expression system, impeded cell cycle re-entry. This indicates a bi-directional relationship whereby HES1 is regulated by, but also regulates, the cell cycle. Together, our findings suggested that unperturbed HES1 dynamics are required for successful re-entry from cell cycle arrest and that interfering with HES1 dynamics may have therapeutic relevance towards managing dormant tumour cells.

Results

Modelling reversible cell cycle arrest with CDK4/6 inhibition

To capture single-cell HES1 protein expression oscillations it is necessary to perform multi-day quantitative live-imaging, with high temporal resolution. This is currently implausible *in vivo*, therefore it was necessary to develop an *in vitro* system to model ER+ breast cancer dormancy. Due to the capacity for CDK4/6 inhibitors to invoke reversible G0/G1 arrest *in vitro* (Trotter *et al*., 2020; Crozier *et al*., 2022), we reasoned that they could be used to mimic the fundamental cell cycle features of entry into and exit from arrest observed during dormancy and reactivation.

To assess the impact of the CDK4/6 inhibitor, palbociclib, on the proliferation of an ER+ breast cancer cell line, MCF-7 cells were incubated with palbociclib for 4 days before being either released into growth media or maintained in palbociclib. These cells were then monitored at the population-level for a further 10 days. Longitudinal growth-curve analyses showed that tissue growth was inhibited and this inhibition was maintained long-term by palbociclib (Fig. 1A). Importantly, the cell cycle arrest induced by palbociclib appeared to be highly-reversible. Following release from Palbociclib on day 4, population-level growth resumed within one day and reached the same fold-change increase in confluence as the treatment-naïve condition by day 14 (Fig. 1A).

We also analysed several molecular indicators of cell cycle progression. Immunostaining for the proliferation marker, Ki67, which stains cells in the late-G1, S, G2 or M phases of the cell cycle (Miller *et al*., 2018), revealed that the proportion of cells in these phases was significantly reduced following 3-day treatment with palbociclib but recovered 24h post-release, indicating a reversible G0/early-G1 arrest (Fig. 1B-C). Similarly, decreased incorporation of the nucleoside analogue, EdU, indicated a reduction of cycling through S-

Phase in response to CDK4/6 inhibition which was partially recovered 24h following palbociclib withdrawal (Fig. 1D). This was further consistent with single-cell measurements of mitosis frequency during live-imaging using a HES1 reporter as a nuclear marker (Fig. 1E; reporter shown in Fig. 2A). Mitoses were identified based on nuclear envelope breakdown, diffusion of HES1 into the cytoplasm and subsequent cytokinesis (inset, Fig. 1E). This revealed that 85% of cells divided within 30 hours of release from palbociclib (Fig. 1F). A baseline rate of continued divisions was observed in the unreleased cells, indicating incomplete arrest. Released cells proceeded largely synchronously from G0/G1 arrest to division, as previously reported in other cell lines (Trotter *et al*., 2020), reaching mitosis most commonly ~18-19h following palbociclib removal (Fig. 1E, G). This cell-cycle synchronicity is not ordinarily observed in proliferative MCF-7 culture (Sabherwal *et al*., 2021) and was quickly lost over subsequent generations in the released cells. Together, these data indicate that palbociclib can be used to readily induce reversible G0/1 arrest in MCF-7 cells, in a manner that is amenable to single-cell live-imaging experimentation.

HES1 ~24h protein expression oscillations are missing in arrested cells

Prior to investigating whether HES1 protein expression oscillations are implicated in breast cancer cell cycle control, it was first necessary to determine how HES1 protein dynamics are altered during cell cycle arrest. To achieve this, MCF-7s expressing an endogenous HES1 fusion reporter (mV-HES1) were used (Fig. 2A). This cell line was previously engineered via CRISPR-based in-frame knock-in of an mVenus fluorophore at the HES1 N-terminus in MCF7s, creating a direct fusion of mVenus to HES1, allowing real-time live observation of HES1 protein expression in single cells (Sabherwal *et al*., 2021). An additional reporter cell line featuring mVenus protein fused to a nuclear localisation signal and driven by a constitutive promoter (UBC-mV-NLS) served as a control for non-oscillatory expression (Fig. 2A; Fig. S1).

Proliferative cells exhibited the previously-characterised features of periodic HES1 expression, demonstrating oscillations at the single-cell level (Fig. 2B), which were asynchronous across the population (Fig. S2A-B). Specifically, these oscillations were correlated with cell cycle progression such that in most cells, HES1 expression is high at the beginning of a cell cycle, then the level temporarily declines prior to S-phase, before accumulating again during G2,

reaching a second high level prior to mitosis (Fig. S2C). Viewed over consecutive cell divisions this cell cycle-correlated oscillation was found to have a median periodicity of 23-25h using Lomb-Scargle Periodogram (LSP) (Fig. 2C) and Autocorrelation Function (ACF) analysis pipelines (Fig. S3). This is consistent with our previous report (Sabherwal *et al*., 2021) and matches the average length of the cell cycle in these cells. The term 'circadian-level' is used to describe this circa 24h periodicity herein, without implying a specific causative connection to the circadian clock. Further in line with our earlier findings, shorter ultradian-level periodicity was also contained within HES1 time series from proliferative cells, which was apparent when the traces were detrended to remove the longer periodicity (Fig. 2B). These nested ultradian oscillations demonstrated a median periodicity of 6-7h (Fig. 2D). Simultaneous quantitative live-imaging of palbociclib-treated and vehicle-treated control (DMSO) mV-HES1 cells suggested that the longer, circa 24h, periodicity in HES1 expression level disappeared in palbociclib-treated cells (Fig. 2E).

LSP analysis was used to measure the relative power of oscillations across different frequencies in each experimental condition (Fig. 2F-I). Proliferative mV-HES1 traces exhibited prominent oscillations in the circadian frequency range (20-30h), that were significantly more powerful than non-oscillatory control UBC-mV-NLS time-series (Fig. 2F-G). Interestingly, the strength of circadian-range HES1 oscillations were significantly reduced in palbociclib-arrested mV-HES1 cells, falling below the power of aperiodic UBC-mV-NLS controls, indicating that circadian-level HES1 periodicity is lost during arrest.

While a prominent peak around 25h was observed in the power spectrum of proliferative mV-HES1 cells (Fig. 2F), indicating strong consensus circadian-level periodicity, no clear peak was observed in the ultradian range of these cells (Fig. 2H). Indeed, the power of mV-HES1 ultradian oscillations in proliferative cells was not significantly distinct from UBC-mV-NLS control values (Fig. 2I), suggesting that they cannot be reliably distinguished from the noisy fluctuations of the control. However, the power of HES1 ultradian oscillations was enhanced in arrested cells, rising above the power of UBC-mV-NLS controls. The fact that HES1 ultradian oscillations are sub-detectable in proliferative cells and are enhanced in arrest likely indicates they are not important in the context of normal cell cycle progression. This is consistent with

our previous report which did not find any correlation between ultradian HES1 oscillation parameters and cell cycle duration (Sabherwal *et al*., 2021).

In addition to the CDK4/6i model of arrest, time-series from spontaneously non-dividing (SND) mV-HES1 cells in proliferative culture were also analysed (Fig. S4A-B). Identical changes to HES1 periodicity were observed in this unperturbed setting, with reduced circadian-level (Fig. S4C-D) and enhanced ultradian oscillations (Fig. S4E-F) observed in SND cells, indicating these periodicity changes are a common feature of arrest, rather than a specific consequence of CDK4/6 manipulation.

Together, these data show that circadian-level HES1 oscillations are prominent in dividing cells and are lost during cell cycle arrest, suggesting that they may be driven by the cell cycle.

HES1 is maintained at a higher level exhibiting smaller dips during arrest

We previously determined that the trough of the circadian-level trend (termed the dip herein), while variable in absolute timing between cells, reliably preceded S-phase in each cell. Moreover, this dip occurred at a set interval of approximately 10-14 hours prior to the next cell division. The finding of a fixed time interval between the HES1 dip and mitosis in proliferative cells was replicated here (Fig. 3A-B). However, in palbociclib-treated cells, the timing of the HES1 minimum dip in individual cells was distributed evenly across their time series, in an unpredictable manner (Fig. 3A-B), in direct contrast to control proliferative cells.

We hypothesised that, if the HES1 dip is important for G1/S progression it may be less prominent in G0/G1 arrested cells where S-phase progression is inhibited. To test this, we examined whether the amplitude (peak minus trough) and fold-change (peak divided by trough) of randomly timed dips present in single-cell time-series of arrested cells were of similar magnitude to the G1/S dips in proliferative cells. This revealed that the ultradian HES1 dips of arrested cells exhibited reduced fold-change and amplitude compared to circadian-level G1/S dips from proliferative cells (Fig. 3E-F), indicating that HES1 is less variant in arrested cells.

In proliferative cells, the fold-change and amplitude of ultradian dips are significantly smaller than circadian-level G1/S dips in the same cells (Fig. 3E-F). This is consistent with the observation that circadian-level oscillations are the dominant frequency in proliferative cells (Fig. 2F-I). During arrest, the amplitude of ultradian dips is increased (Fig. 3F), in line with the enhancement of ultradian periodicity (Fig. 2I), but this amplitude is still smaller than G1/S dips in proliferative cells.

In addition to modulating HES1 dynamics, palbociclib treatment increased HES1 expression, with a 1.9-fold rise in mRNA levels by RT-qPCR (Fig. 3G) and a 1.4-fold increase in mean protein levels based on single-cell live imaging of mV-HES1 cells (Fig. 3H). This effect was specific to HES1, as no change was observed in control UBC-mV-NLS cells (Fig. 3H). Moreover, HES1 protein was also upregulated 1.4-fold in SND cells compared to proliferative counterparts (Fig. S4G), indicating this is not solely a direct effect of palbociclib treatment but extends to unperturbed models of arrest as well. Notably, while palbociclib raised mean HES1 protein levels, these remained within the normal dynamic range observed during cycling. Mean levels in arrested cells were not significantly different from the maximum levels seen in proliferating cells (Fig. 3I). The increase in maximum HES1 intensity during arrest was modest (1.1-fold), whereas the minimum intensity rose more substantially (1.6-fold) compared to controls. These data indicate that palbociclib elevates the baseline, rather than the maximum, HES1 expression. Thus, palbociclib maintains HES1 at the highest levels normally seen in proliferating cells, preventing their decline rather than increasing it beyond the physiological range.

Together, the data indicates that HES1 oscillatory dynamics are profoundly altered during cell cycle arrest, manifested primarily as a loss of the circadian-level, cell cycle-associated, oscillations. Additionally, HES1 is maintained at a moderately elevated level (1.4-fold) and exhibits less pronounced dips compared to cycling cells.

HES1 circadian-level oscillations return upon cell cycle re-entry

To determine whether circadian-level HES1 oscillations could be rescued by cell cycle re-entry, arrested mV-HES1 cells were released from palbociclib treatment into growth media and then

continuously monitored by single cell live-imaging, beginning approximately one hour later. (Fig. 4A). A PCNA-based cell cycle reporter (Fig. 4B), which exhibits a punctate pattern while cells are in S-Phase (Zerjatke *et al*., 2017), was used to visualise the G1/S transition following release from arrest (Fig. 4C). Circadian-level oscillations returned in released cells, demonstrating the characteristic cell cycle-associated HES1 dynamics, typified by peaks around mitoses, interspaced by G1/S dips (Fig. 4D). This was supported by periodogram analysis (LSP), which showed that time-series from released cells exhibited increased power within the circadian frequency range compared to both unreleased counterparts and control UBC-mV-NLS cells under either condition (Fig. 4E–F). Periodicity estimations by ACF and LSP indicated a circadian-level dominant period of 22-26h, similar to proliferative DMSO-controls (Fig. S5A). Ultradian oscillations were of reduced power in released cells compared to unreleased controls (Fig. S5B). Moreover, the size of dips were significantly increased in released cells compared to unreleased counterparts (Fig. S5C-D), signifying a reversal of the previously observed effect where dips became smaller upon the induction of arrest (Fig. 3E-F).

Interestingly, a pronounced HES1 dip was reproducibly observed at the beginning (~8-10h post-release) of individual released cell time-series (Fig. 4G). This specific first dip had an average fold-change of 2.2, which was significantly greater than any dip seen in the same time period of time series from unreleased control cells or control UBC-mV-NLS cells released into growth media (Fig. 4H). This is consistent with the fact that palbociclib instructs a G0/G1 arrest and thus released cells must next flux into S-phase, which has been shown to follow a HES1 dip. The PCNA cell cycle reporter was used to confirm that the HES1 dip seen upon release precedes, or coincides with, S-Phase (Fig. 4D).

A dip was also observed within the first 10h of time-series from palbociclib-arrested mV-HES1 cells (Fig. 4D, H), which likely reflects a transient response to serum stimulation, as HES1 is a serum-inducible gene (Yoshiura *et al*., 2007) and fresh serum is introduced at the time of media change. Nevertheless, the fold-change of the dip detected in released cells was significantly greater than that of those maintained in palbociclib (Fig. 4H), implying an additional source of levels decline, beyond the serum response, which can be attributed to the G1/S transition. In addition, HES1 mean protein levels were found to descend upon release

(Fig. 4I), reversing the elevation detected during arrest (Fig. 3H). Levels of mVenus protein in UBC-mV-NLS cells were unaffected by release (Fig. 4I).

These experiments reveal that circadian-level HES1 oscillations are a hallmark feature of cell cycle progression, which are not observed in arrested cells but can be rescued by re-entry. Moreover, these data establish that the characteristic G1/S HES1 dip is observed during the process of cell cycle re-entry. Taken together, these findings suggest a reciprocal interaction of HES1 and the cell cycle, whereby the cell cycle shapes HES1 dynamics and the HES1 dip observed in proliferative cells may be required for G1/S transition.

Sustained expression of HES1 prior to release impedes cell cycle re-entry

To examine whether the HES1 dip is functionally required for S-phase during cell cycle re-entry, a Tet-On based inducible system of sustained HES1 expression was generated (Fig. 5A). Tet-mS-HES1 expression was expected to be constitutive (aperiodic) once induced and to override the expression from the endogenous HES1 by virtue of HES1 acting to repress expression from its own promoter, as previously described (Marinopoulou *et al*., 2021). However, it was discovered that Tet-mS-HES1 expression was unexpectedly dynamic, demonstrating prominent oscillations, when imaged at the single cell level (Fig. S6A, C). These oscillations were asynchronous at the population level, but the expression was anti-correlated with the endogenous mV-HES1 protein at the single cell level, as may be expected by the cross-repression of the endogenous HES1 promoter by exogenous Tet-mS-HES1.

We reasoned that the anti-corelated dynamics of endogenous and exogenous HES1 expression, where one reporter compensates when the other declines, creates a near-sustained expression of HES1, shortening the time that HES1 spends in the low state of expression. In addition, the overall expression level of HES1 mRNA was also raised 2-fold at the population level by doxycycline treatment in proliferative Tet-mS-HES1 cells and 1.4-fold in arrested cells (Fig. S6B). Thus, this system can be used to prevent the normal dips in HES1 expression and increase levels at specific temporal moments, allowing inference of the role of regular HES1 cell cycle dynamics.

First, to investigate whether the HES1 dip is necessary for re-entry into the cell cycle from arrest, sustained HES1 expression was induced at the point of release from palbociclib (Fig. 5B). This was performed to maintain HES1 levels as cells attempt to re-enter the cell cycle, thereby preventing the dip that is usually observed around G1/S. Indeed, anti-correlated expression of Tet-mS-HES1 and endogenous mV-HES1 was observed in time-series from this assay, effectively amounting to sustained expression (Fig. S6C). This sustained expression of HES1 at the point of release markedly impaired cell cycle re-entry, characterised by a dramatic reduction in the number of cells which successfully divided in the first 24 hours following release, from 75% in unperturbed cells to 14% (Fig. 5C-D). Addition of doxycycline had no effect on the re-entry rate of parental mV-HES1 cells lacking the Tet-mS-HES1 cassette (Fig. 5D). The minority of cells which divided during this 24h time-course (14%), all showed a synchronous decline in HES1 expression, manifesting in a visible dip in the mean trace at around 12-15h post-release. This was true both when exogenous Tet-mS-HES1 expression was considered alone (Fig. 5E) or when the exogenous and endogenous signals were aggregated into a single time series to estimate total HES1 dynamics (Fig. 5F). This dip appeared strongly reminiscent of the endogenous HES1 dip ordinarily observed during G1/S upon re-entry.

In contrast, the mean trace of cells which did not re-enter the cell cycle did not reproduce this pattern. The mean trace appeared largely flat at the population level, either when tracking Tet-mS-HES1 alone (Fig. 5E) or the aggregated endogenous and exogenous signals (Fig. 5F), showing that a synchronised dip in HES1 was not observed in this group. In spite of individual cell variation, a greater proportion of cells remained positive for Tet-mS-HES1 expression throughout the time-course in the non-dividing cohort compared to the dividers, during the 24h window of observation (Fig. 5G). Moreover, the fold-change of the aggregated signal from the point of release to the time of minimum intensity was significantly higher in cells which managed to re-enter the cell cycle (5.8x), compared to those which were blocked from re-entry (1.9x) (Fig. 5H). This supports the notion that a more prominent dip in total HES1 is observed when a cell successfully re-enters the cell cycle compared to cells which are blocked. Together, the data suggest that the HES1 G1/S dip is necessary for efficient cell cycle re-entry after the release from palbociclib-induced arrest.

We next investigated whether sustained HES1 expression could block cell cycle re-entry beyond 24 hours post-release. To do this, we performed population-level growth curve analysis for 7 days following palbociclib withdrawal (Fig. 5I–J). Induction of sustained HES1 expression with doxycycline prior to release prevented population outgrowth (Tet-mS-HES1, release, Fig. 5I). Notably, palbociclib-arrested and released cultures displayed negative growth slopes from approximately day 3 of the time-course, suggestive of a net reduction in cell number due to cell death. Consistent with this, we observed dose-dependent cell death in Tet-mS-HES1 cells exposed to escalating doxycycline concentrations following release (Fig. S7A–B). Interestingly, sustained HES1 had no significant effect on the growth rate of proliferative (DMSO) cells, suggesting that arrested and cycling cells may differ in their sensitivity to sustained HES1-induced cell death (Fig. 5I–J). Importantly, doxycycline treatment did not affect population growth in control cells expressing an inducible mScarlet-NLS reporter (Tet-mS-NLS), across all experimental conditions (Fig. 5I–J). Together, these results suggest that sustained HES1 expression at the time of release from G0/G1 arrest impairs cell cycle re-entry, induces cell death and limits subsequent population expansion.

Discussion

The work we describe in this paper is relevant to the clinical issue of tumour recurrence in ER+ breast cancer. While recurrence is a multifactorial process involving interaction of DTCs with the TME, here we have focused on the fundamental process of quiescent cancer cells re-entering the cell cycle at the single-cell level, which underlies relapse initiation. While such cancer cell re-activation events can happen stochastically (Rosano *et al*., 2024), here, we have specifically addressed the cell-cycle re-entry which takes place when the cell cycle inhibitor, palbociclib, is removed. This is of clinical relevance because, although palbociclib and related CDK4/6 inhibitors are used in the clinic to inhibit cancer cell proliferation, tumours eventually develop resistance and escape their cytostatic effects. Although our model involves CDK4\6 inhibition withdrawal, our findings may be more widely applicable to the emergence from quiescence.

Complementing previous studies (Sabherwal *et al*., 2021), we found that the nuclear protein concentration of Notch target HES1, assayed with live imaging in proliferative MCF-7 cells, exhibits a dynamic pattern, comprising nested oscillations of 2 distinct frequencies: a circadian-level oscillation with an average periodicity of 23-25 hours, and an ultradian oscillation with a periodicity of 6-7 hours. The circadian-level oscillations match the length of the average cell cycle, are dominant in proliferative cells, are lost during arrest and resume upon cell cycle re-entry, indicating that they are driven by the cell cycle.

Conversely, ultradian HES1 oscillations are unlikely to have a role in cell cycle regulation because, unlike the circadian-level oscillations, they don't have a reproducible association with cell cycle phase, are not significantly different than noisy control fluctuations in proliferative cells. We suggest they are simply the product of HES1 autorepression coupled with mRNA and protein instability, which has been shown to generate autonomous ultradian oscillations across many molecules, including HES1 (Monk, 2003; Bonev *et al*., 2012; Webb *et*

al., 2016; Phillips *et al*., 2017; Minchington *et al*., 2020) . In addition, the troughs of HES1 in ultradian oscillations may be too short for downstream targets to be regulated, as has been postulated for Her6 (Soto *et al*., 2020*)* and p53 oscillations (Harton *et al*., 2019). The enhancement of the ultradian frequency in arrested cells is likely an indirect effect of the loss of circadian-level oscillations, because in nested oscillation systems, the phase of the slower oscillator can modulate the amplitude (or prominence) of the faster one (Penny *et al*., 2008).

In a developmental context, HES1 oscillations can be cell autonomous (Webb *et al*., 2016), but in a multicellular environment, they are most likely coupled to other cells by virtue of Notch signalling which provides a positive input to HES transcription (Biga *et al*., 2021; Doostdar *et al*., 2024). Notch signalling can link HES1 regulation not only to environmental cues but also to the cell cycle. Specifically, the Notch intercellular domain (NICD) has been shown to be phosphorylated by CDK2 leading to degradation during S-phase (Carrieri *et al*., 2019). This may periodically interrupt stimulation of HES1 transcription by Notch and generate the observed G1/S dip to the HES1 protein concentration. Furthermore, post-translational modifications by the cell cycle machinery could also directly regulate HES1 protein stability, as has been shown in *Xenopus* (Hardwick *et al*., 2019), where phosphorylation of conserved sites by CDK4 and CDK2 promotes HES1 protein degradation. This may explain why palbociclib treatment, which inhibits both CDK4/6 directly and CDK2 indirectly (Pack *et al*., 2021), abolished circadian-level oscillations and elevated protein levels, by virtue of increased HES1 protein stability.

In addition to showing that circadian-level HES1 oscillations are driven by the cell cycle, we report that these oscillations in turn regulate cell cycle progression, as predicted by previous theoretical work (Rowntree *et al*., 2022). This conclusion is supported by the fact that preventing the HES1 dip normally observed prior to S-phase entry, via sustained HES1 expression, impeded cell cycle re-entry from arrest.

Key mechanistic questions emerging from this work are how HES1 oscillations regulate the cell cycle in proliferating cells and how sustained HES1 impedes cell cycle re-activation. HES1 is a known transcriptional repressor of both activators (CycD1, CycE2, CycA2 and E2F) and inhibitors of the cell cycle (p21, p27) (Castella *et al*., 2000; Hartman *et al*., 2004; Murata *et al*.,

2005; Noda *et al*., 2011; Pfeuty, 2015; Cenciarelli *et al*., 2017). We might infer that the function of the HES1 oscillation in proliferating cells is to allow de-repression of cyclins via the dip in its level of expression that precedes the G1/S transition. In addition, the high level of HES1 in G1 may repress p21 and p27, to allow S-phase entry.

When HES1 is sustained, cyclins may be continuously inhibited at the transcriptional level, thus preventing cell cycle progression. Moreover, recent work in murine NSCs has discovered that sustained HES1 upregulates p21 (Marinopoulou *et al*., 2021), which is indirect, via repression of a p21 repressor (Maeda *et al*., 2023). While these ideas remain to be fully elucidated in human breast cancer, we surmise here that sustained HES1 expression may have the effect of both repressing cyclins and activating p21. This would lead to effective inhibition of re-entry into the cell cycle by virtue of a double-block, which would maintain the cell cycle blockade when CDK4\6 inhibitors are removed or are no longer effective, such as is seen in resistance. We also found that spontaneously quiescent cells exhibited the same dynamic changes to HES1 as those arrested by palbociclib, suggesting they may exhibit similar vulnerabilities that can be exploited.

Due to the fact that the Tet-On sustained HES1 system changed both the dynamics of total HES1 as well as increased the levels, it remains difficult to disentangle the relative effects of each change. Although, we do note that during both palbociclib-mediated and spontaneous arrest, the increase in mean HES1 protein levels is modest (1.4-fold) and not outside the physiological range seen in proliferative cells, indicating that HES1 levels do not have to be dramatically increased during arrest.

In addition to manipulating cell cycle progression, we observed that sustained HES1 induced cell death. Previous findings in *Xenopus* neural development reported that increasing stability of the HES1 orthologue induced apoptosis via a p53-mediated pathway (Bonev *et al*., 2011), similar mechanisms could explain the observed cell death here. Intriguingly, sustained HES1 expression induced negative population growth rates in both arrested cultures and those released from arrest. This may be of significant clinical benefit, because current therapeutic options predominantly target proliferative cells. Thus, manipulating HES1 dynamics may offer a novel strategy to eliminate quiescent cancer cells, clear residual disease and impede

reactivation. However, as this work was conducted in simplified 2D *in vitro* models, further validation in more physiologically and therapeutically relevant systems, such as PDX tumours, will be essential prior to translation.

In conclusion, we found that the expression dynamics of the Notch pathway transcription factor, HES1, changed dramatically and reversibly during entry into and exit from cell cycle arrest. These changes are functionally important, as their perturbation prevented reactivation. Our findings suggest that targeting protein dynamics may offer a promising and precise strategy to prevent emergence from dormancy in breast cancer. Understanding how to block quiescent cancer cells from re-activation complements other approaches aimed at pushing cancer cells into quiescence.

Materials and Methods

Cell Culture

MCF-7 cells were cultured in high-glucose DMEM (D6429, Sigma) supplemented with 10% heat-inactivated FBS (10500064, Gibco) and maintained at 37°C with 5% CO_2 in a humidified incubator. Cells were routinely tested for mycoplasma and typically passaged twice per week.

For cell cycle arrest, cells were treated with 1 µM palbociclib (PZ0383, Sigma) or an equal volume of DMSO (D8418, Sigma) for 3–4 days. For release, cells were washed with pre-warmed PBS (2–3 min) and replaced into growth media containing DMSO instead of palbociclib. Unreleased controls received fresh palbociclib-containing media. Doxycycline was added at 5 or 50 ng/mL (as indicated) (D9891, Sigma), 24 h after palbociclib addition (Day 1) and again at release (Day 3).

Reporter Constructs and Cell Lines

The constitutive nuclear mVenus reporter UBC-mV-NLS, driven by the Ubiquitin C promoter, was used as a live-imaging control (Sabherwal et al., 2021). The PCNA-based S-phase reporter from our previous study (Sabherwal et al., 2021) was modified by replacing mCherry with mTagBFP2 to generate UBC-BFP-PCNA.

To modulate HES1 expression dynamics, we used a second-generation Tet-On system (VectorBuilder), comprising two lentiviral plasmids:

1. PGK-tTS-T2A-rtTA — expressing the tetracycline transcriptional silencer (tTS) and the reverse tetracycline-controlled transactivator (rtTA), separated by a T2A peptide under the PGK promoter. Also contains blasticidin resistance gene driven by PGK.

2. TRE-mS-HES1 or TRE-mS-NLS — expressing mScarlet (mS) fused to either full-length HES1 or a nuclear localization signal, under control of the tetracycline-responsive element promoter (TRE). Also contains neomycin resistance gene driven by PGK.

MCF-7 cells previously engineered via CRISPR-Cas9 to express an mVenus-HES1 fusion protein (mV-HES1) (Sabherwal et al., 2021) were further modified to express UBC-BFP-PCNA, PGK-tTS-T2A-rtTA, and either TRE-mS-HES1 or TRE-mS-NLS, yielding Tet-mS-HES1 and Tet-mS-NLS cell lines. Parental MCF-7 cells were also transduced with UBC-mV-NLS to generate a control line.

Lentivirus Production and Transduction

All reporter constructs were packaged into lentivirus using HEK-293-LTV cells (LTV-100, Biolabs). Two T75 flasks were seeded with 700,000 cells each and cultured for 72 h. Transfections were performed by combining 54 µL 1× PEI (919012, Merck) in 500 µL serum-free media (D1145, Sigma) with a DNA mix containing 6 µg MD2.G, 9 µg psPax2, and 12 µg lentiviral expression plasmid in another 500 µL of serum-free media. After 2 min (PEI) and 30 min (combined mix) of incubation at room temperature, 500 µL of the final solution was added dropwise to each flask.

After 24 h, media was replaced with 10 mL fresh growth medium supplemented with 10 mM sodium butyrate (19137, Sigma) and incubated for 6–8h. Medium was then replaced again, and virus-containing supernatant was collected 40–48h later, filtered (0.45 µm), and mixed with 5 mL 5× PEG virus precipitation solution (LV810A-1, SBI). The solution was incubated at 4°C for 24–96 h, centrifuged at >1,500 × g for 30–60 min, and resuspended in 200 µL chilled PBS. Aliquots were stored at –80°C.

For transduction, 100,000 MCF-7 cells were seeded per well in a 6-well plate, then infected with one aliquot of virus in 1 mL media containing 0.1% polybrene (TR-1003-G, Sigma). After 24–48h, cells were selected with 20 µg/mL blasticidin (15205, Sigma) or 5 mg/mL G418 (4727878001, Sigma) for 72h, followed by recovery in standard growth media. Fluorescent populations were enriched by FACS using a Bigfoot Spectral Cell Sorter (Thermo) operated by the Flow Cytometry Core Facility, University of Manchester.

RNA Extraction and RT-qPCR

Total RNA was extracted using the RNeasy kit (74104, Qiagen), and 250 ng of RNA was reverse-transcribed using SuperScript III Reverse Transcriptase (18080044, Thermo). Resulting cDNA was diluted 1:10, corresponding to ~25 ng RNA per qPCR reaction. qPCR was performed using Power SYBR Master Mix (4367659, Thermo). Only technical replicates within 0.1 CT of each other were included in the analysis. Gene expression was normalized to housekeeping genes (GAPDH and ActinB or Rpl7) by calculating ΔCT, and relative expression was determined as 2^–ΔCT. Where indicated, values were further normalized to the median of a designated control condition to estimate fold change.

Immunostaining and Immunofluorescence Microscopy

Cells were seeded on glass coverslips at 5,200 cells/cm² and treated with 1 µM palbociclib (PZ0383, Sigma) or DMSO (D8418, Sigma). On Day 3, selected wells were released into DMSO-containing media. At endpoint, cells were fixed with 4% PFA/PBS and permeabilised using 0.5% Triton X-100 in PBS. Primary antibody incubation was performed overnight at 4°C, followed by secondary antibody incubation for 2h at room temperature in the dark. Antibodies were diluted in 1× Western Blocking Reagent (Sigma) in PBS. Nuclei were stained with 1 µg/mL DAPI (62248, Thermo), and coverslips were mounted using ProLong Diamond Antifade Mountant (P36934, Invitrogen). Primary antibody was mouse anti-Human Ki67 (1:100, 550609, BD Biosciences) and secondary antibody was goat anti-mouse Alexa Fluor 568 (1:1000, A11004, Invitrogen).

Images were acquired using an Olympus IX83 inverted microscope (10× objective) equipped with an Orca ER camera (Hamamatsu) and CellSens software (Olympus). Custom Fiji macros were used for batch image preprocessing. Quantification of Ki67+ nuclei was performed using a MATLAB pipeline (Marinopoulou et al., 2021) involving DAPI-based segmentation, followed by intensity extraction per nucleus. Ki67+ cells were defined as those exceeding the fluorescence threshold set by secondary-only controls.

IncuCyte Imaging and Population Growth Analysis

Cells were seeded at 2,850 cells/cm² in 12-well plates and treated with DMSO, palbociclib, or doxycycline (D9891, Sigma) as required. Immediately following treatment, plates were placed

into the IncuCyte Zoom live-cell imaging system (Essen Biosciences). Whole-well 4× phase contrast images were acquired every 3–12h over 10–14 days. Treatments and releases were performed in tissue culture between scans. All wells were subject to the same handling, including media replacement and washes, to control for serum-related effects.

Image analysis was conducted using IncuCyte software, which applied cell line-specific segmentation masks to estimate percentage confluency. Confluency was normalised either to the initial seeding density or to the confluency at release to allow fold-change comparison. Growth curves represent the mean of experimental replicates, with shaded areas indicating standard deviation. To test statistical significance, confluency measurements from the final 24h of the time course were pooled and compared across conditions.

EdU Incorporation and Flow Cytometry

MCF-7 cells were seeded at 5,200 cells/cm² in 6-well plates and treated with either DMSO, palbociclib continuously, or palbociclib for 3 days followed by release. On Day 3, 2.5 µM EdU (5-Ethynyl-2'-deoxyuridine) was added during the media change or release. After 24h, cells were harvested and processed for EdU detection using the Click-iT Plus Flow Cytometry Kit (C10634, Thermo), following the manufacturer's instructions. Samples were analysed using an LSRFortessa SORP flow cytometer (BD Biosciences).

Quantitative Single-Cell Live Imaging and Tracking

Cells were seeded in 4-compartment glass-bottom dishes (627870, Greiner) and imaged within the chamber of a Zeiss LSM880 inverted confocal microscope maintained at 37 °C and 5% CO_2. Using a 20× objective with 0.6x zoom, 2×2 grid live images were acquired every 20 min for up to 96 h, depending on the experiment. Z-stacks spanning ~40 µm (typical nuclear signal range: 30–35 µm) were captured and collapsed via maximum intensity projection. Resulting time-lapse movies were manually tracked using Imaris (Bitplane) by placing 9 µm diameter spots (to cover majority of nucleus) over individual cells to capture nuclear fluorescence. Manual tracking was utilised due to the necessity to track cells over divisions, which is often poorly performed by automated approaches. Moreover, due to oscillations of HES1, nuclear signal intensity often reached a nadir which automated algorithms struggled to detect. Introduction of a constitutive nuclear marker to circumvent

this was limited by available fluorescent channels. Cells were typically tracked from mitosis to mitosis, to identify cell cycle periodicities, unless stated otherwise.

DMSO-treated control cells were tracked for at least two full generations to capture recurring dynamics. In palbociclib-treated conditions, cells were tracked for the full movie duration, rare dividing cells under palbociclib arrest conditions were excluded. In release experiments, cells were tracked from the first frame until at least two mitoses post-release were observed. Tracking data including x, y, z coordinates, mean nuclear fluorescence intensity, and time were exported from Imaris and processed using *tRecs*, a custom Python script (https://github.com/TMinchington/tRecs), which provides information on lineages and mitotic events. Aggregated master files were then imported into MATLAB or RStudio for downstream analysis.

Time-Series Visualisation and Protein Level Estimation

Nuclear protein levels were represented by the mean fluorescence intensity of each manually placed spot. Time-series were imported into RStudio and Z-score normalised per cell (mean trace intensity value was subtracted from the raw value at each timepoint and divided by the standard deviation). This normalisation was performed to control for differences in fluorescent intensity levels between individual cells For comparison of expression dynamics between mVenus and mScarlet reporters in the same cell, each trace was additionally min–max scaled to a 0–1 range based on that cell's minimum and maximum expression values, allowing relative trace shapes to be visualised on the same scale. The time plotted refers to time since the track started rather than when the movie started so is independent to each cell. This is predominantly the time since the first mitosis of the track for proliferative cells, or the start of the movie for palbociclib-arrested and released cells.

S-phase events were manually annotated based on punctate UBC-BFP-PCNA signals (Zerjatke *et al*., 2015) and incorporated into trace metadata. Visualisation was performed in RStudio using *ggplot2* from the *tidyverse* library (https://www.tidyverse.org/). Mean traces were constructed by aggregating Z-scored values and plotting the average with standard deviation across aligned timepoints.

To assess population-wide dynamics, individual Z-scored traces were visualised as heatmaps using *geom_tile* in *ggplot2*, where each column represented a cell and colour denoted fluorescence intensity. For DMSO-treated two-generation tracks, time was aligned to the third and final mitosis; for palbociclib-arrested cells, alignment was to the endpoint of the time series.

Protein abundance between conditions was estimated by calculating the mean raw nuclear fluorescence intensity of each cell trace in RStudio and visualised via box plots across experimental replicates. Minimum and maximum intensities for each trace were also quantified.

Spontaneous Non-Divider Dataset

mV-HES1 cells were cultured in standard growth media and continuously live-imaged for up to five days. Amidst these proliferative conditions, a subset of cells exhibited extended periods without division, including some that remained non-proliferative throughout the entire time-course. Cells that failed to divide for at least 60 hours, exceeding the average duration of two generations (57h), were classified as spontaneous non-dividers (SNDs). Time-series from SNDs were compared to mother-daughter traces from actively cycling cells from the same culture and analysed for differences in mV-HES1 periodicity.

Single-Cell Live Imaging Re-Entry Assay

To quantify single-cell cell-cycle re-entry following palbociclib release, a live-imaging assay was performed. The number of cells present at the start of the time-course was manually counted. Re-entry events were manually assigned upon entry into mitosis phase, characterised by translocation of HES1 from the nucleus to the cytoplasm, due to nuclear envelope breakdown (as in Fig. 1E). In the release condition, only the first division per lineage was counted as a re-entry event to avoid false inflation from subsequent divisions within the same lineage. For example, a cell dividing at 1 h and again at 23 h post-release would otherwise be misclassified as two independent re-entries. In actuality, any cells which divided 1h following release were likely not arrested in the first place as we have previously shown mitosis occurs around 10-14 hours after G1/S (Sabherwal *et al*., 2021). There were no instances of multiple divisions observed within the same lineage in the palbociclib control condition.

In the Tet-mS-HES1 re-entry assay, cells were classified as Tet-mS-HES1 positive if their mScarlet fluorescence exceeded a threshold set by the maximum extra-cellular background intensity in the image. All mScarlet-positive were then followed for 24h (based on the average time of re-entry defined in the earlier assay) and manually assigned to one of three potential fates: division, no division or death. Cell death was identified based on characteristic morphology and behaviour, including increased autofluorescence, loss of motility, nuclear shrinkage, membrane blebbing, and cessation of proliferation. In control cell lines lacking Tet-mS-HES1 (and thus mScarlet), a random subset of cells was followed independent of fluorescence. The mean percentage of non-dividing cells was calculated across biological replicates.

Time Series Dip Size Quantification

To quantify the magnitude of periodic dips in fluorescence intensity time-series, a custom MATLAB pipeline was developed. Peaks and troughs were detected using the *findpeaks* function, which returns both the amplitude and time index of features in the trace. Troughs were identified by applying the same function to the vertically inverted signal and taking the absolute values.

For circadian-level oscillations, traces were smoothed using *smoothdata* with a Gaussian filter and a moving window size of 10h, applied twice for enhanced smoothing. A minimum peak prominence of 0.5 was used to identify relevant features. For ultradian oscillations, the same process was applied using a 1.67h moving window and a minimum peak prominence of 1.5. All peak and trough amplitudes were extracted from the raw data at the corresponding time indices identified in the smoothed trace.

To assess dip magnitude, each peak was paired with its subsequent trough and dip amplitude (peak value – trough value) and fold-change (peak value / trough value) were calculated. In instances where a trace began with a trough, the preceding local maximum was designated as the initial peak, and vice versa for terminal peaks. Distributions of dip sizes were visualised in Rstudio using *ggplot2*.

Endogenous and Exogenous Signal Aggregation

To approximate total HES1 dynamics in mV-HES1 Tet-mS-HES1 cells, time-series data from both reporters were combined. As absolute fluorescence intensities are not directly comparable between the two fluorophores, each signal was first Z-score normalised before summation. This approach provides an estimate of the overall shape of total HES1 dynamics, rather than an exact quantitative measure. To calculate fold-change of the combined trace it was first necessary to transform the normalised time-series, which by definition contains negative values, to a positive time-series. This was achieved by adding the absolute value of the minimum point in each normalised trace to the entire time-series.

Periodicity Analysis Data Preprocessing

Two-generation mother-daughter traces from proliferative DMSO control cells and uninterrupted palbociclib-arrested time-series were imported into MATLAB. All time-series were detrended using the *smoothdata* function. To identify circadian-level periodicity, a gaussian smoothing filter (with a window equal to the trace length which varied between 60-100h) was applied to yield a near-linear trend. This trend was then removed to even out intra and inter-cell intensity differences which may introduce bias to the data and obscure peak detection. For ultradian period quantification, a gaussian filter (10h moving window length) was applied and detrended. This was performed to remove periodicities greater than 10h, including the already-quantified circadian-level trend and reveal the nested ultradian oscillations.

Autocorrelation Function

Autocorrelation Function (ACF) quantifies the similarity of a signal with time-lagged versions of itself. Peaks in the ACF output correspond to repeated patterns, with the time between peaks providing a periodicity estimate. To assess robustness, a bootstrapping approach was used: each trace was randomly shuffled 100 times, and the ACF was computed on each permutation. Only ACF peaks in the original trace exceeding 0.5 standard deviations above the mean of the bootstrapped scores were retained. The mean time lag between these valid peaks was recorded as the periodicity estimate for that trace.

Lomb-Scargle Periodogram

Lomb-Scargle Periodogram (LSP) is a Fourier- and least-squares–based method optimised for non-uniformly sampled time-series data (VanderPlas et al., 2018). Periodograms were generated using the *plomb* function in MATLAB with the normalise flag to scale power by two times the variance of the time-series. Frequency–power spectra were interpolated across cells to generate a condition-wide average periodogram estimate. To better contextualise frequency analysis, the periodograms' x-axes were converted from frequency to period by taking the inverse of frequency. High-power, single-period peaks indicate strong oscillatory periodicity, while low, diffuse peaks reflect weak or aperiodic signals. LSP visualisations were generated using *ggplot2* in RStudio.

To statistically analyse LSP spectra from different signals, the dominant periodicity was extracted by converting the frequency at which the highest power is observed to a period value, on a cell-by-cell basis, by taking the reciprocal of the frequency. Mean power across circadian (20-30h) or ultradian periodicity range (4h-8h) was calculated by filtering for all frequencies which correspond to periodicities within the specified range, across all cells. Then the mean value of power was calculated at each frequency across every cell from all experiments. These mean power values within the specified range were then compared by boxplot in Rstudio using *ggplot2*.

Quantification and statistical analysis

Statistical testing was performed in Rstudio v.4.4.1 using the '*stats*' and '*ggsignif*' libraries. Data was tested for normality using Shapiro-Wilk to select the appropriate test and significance. Statistical testing information, including significance values and sample size, is provided in figure legends.

Acknowledgements

The authors would like to thank the Dave Spiller and James Bagnall from the Bioimaging Facility, FBMH, University of Manchester; David Chapman, Bradley Dean and Gareth Howell from the Flow Cytometry Facility, FBMH; All members of the Papalopulu lab for their comments and discussion. The work was supported by a Cancer Research UK—Engineering and Physical Research Sciences Research Council Multidisciplinary Award grant to N.P. and R.B.C. (DRCMDP-Nov22/100009), a Wellcome Trust Investigator Award to N.P. (224394/Z/21/Z) and a Medical Research Council PhD studentship to O.C.

References

1. Smittenaar, C. R., Petersen, K. A., Stewart, K., & Moitt, N. (2016). Cancer incidence and mortality projections in the UK until 2035. *British Journal of Cancer*, *115*(9). https://doi.org/10.1038/bjc.2016.304

2. Ferlay, J., Colombet, M., Soerjomataram, I., Dyba, T., Randi, G., Bettio, M., Gavin, A., Visser, O., & Bray, F. (2018). Cancer incidence and mortality patterns in Europe: Estimates for 40 countries and 25 major cancers in 2018. In *European Journal of Cancer* (Vol. 103). https://doi.org/10.1016/j.ejca.2018.07.005

3. Pan, H., Gray, R., Braybrooke, J., Davies, C., Taylor, C., McGale, P., Peto, R., Pritchard, K. I., Bergh, J., Dowsett, M., & Hayes, D. F. (2017). 20-Year Risks of Breast-Cancer Recurrence after Stopping Endocrine Therapy at 5 Years. *New England Journal of Medicine*, *377*(19). https://doi.org/10.1056/nejmoa1701830

4. Bushnell, G. G., Deshmukh, A. P., den Hollander, P., Luo, M., Soundararajan, R., Jia, D., Levine, H., Mani, S. A., & Wicha, M. S. (2021). Breast cancer dormancy: need for clinically relevant models to address current gaps in knowledge. In *npj Breast Cancer* (Vol. 7, Issue 1). https://doi.org/10.1038/s41523-021-00269-x

5. Sosa, M. S., Bragado, P., & Aguirre-Ghiso, J. A. (2014). Mechanisms of disseminated cancer cell dormancy: An awakening field. In *Nature Reviews Cancer* (Vol. 14, Issue 9). https://doi.org/10.1038/nrc3793

6. Phan, T. G., & Croucher, P. I. (2020). The dormant cancer cell life cycle. In *Nature Reviews Cancer* (Vol. 20, Issue 7). https://doi.org/10.1038/s41568-020-0263-0

7. Sosa, M. S., Parikh, F., Maia, A. G., Estrada, Y., Bosch, A., Bragado, P., Ekpin, E., George, A., Zheng, Y., Lam, H.-M., Morrissey, C., Chung, C.-Y., Farias, E. F., Bernstein, E., & Aguirre-Ghiso, J. A. (2015). NR2F1 controls tumour cell dormancy via SOX9- and RARβ-driven quiescence programmes. *Nature Communications*, *6*(1). https://doi.org/10.1038/ncomms7170

8. Rosano, D., Sofyali, E., Dhiman, H., Ghirardi, C., Ivanoiu, D., Heide, T., Vingiani, A., Bertolotti, A., Pruneri, G., Canale, E., Dewhurst, H. F., Saha, D., Slaven, N., Barozzi, I., Li, T., Zemlyanskiy, G., Phillips, H., James, C., Gy\Horffy, B., … Magnani, L. (2024). Long-term Multimodal Recording Reveals Epigenetic Adaptation Routes in Dormant Breast Cancer Cells. *Cancer Discovery*, *14*(5), 866–889. https://doi.org/10.1158/2159-8290.CD-23-1161

9. Correia, A. L., Guimaraes, J. C., der Maur, P., De Silva, D., Trefny, M. P., Okamoto, R., Bruno, S., Schmidt, A., Mertz, K., Volkmann, K., Terracciano, L., Zippelius, A., Vetter, M., Kurzeder, C., Weber, W. P., & Bentires-Alj, M. (2021). Hepatic stellate cells

suppress NK cell-sustained breast cancer dormancy. *Nature*, *594*(7864). https://doi.org/10.1038/s41586-021-03614-z

10. Borriello, L., Coste, A., Traub, B., Sharma, V. P., Karagiannis, G. S., Lin, Y., Wang, Y., Ye, X., Duran, C. L., Chen, X., Friedman, M., Sosa, M. S., Sun, D., Dalla, E., Singh, D. K., Oktay, M. H., Aguirre-Ghiso, J. A., Condeelis, J. S., & Entenberg, D. (2022). Primary tumor associated macrophages activate programs of invasion and dormancy in disseminating tumor cells. *Nature Communications*, *13*(1). https://doi.org/10.1038/s41467-022-28076-3

11. Baldominos, P., Barbera-Mourelle, A., Barreiro, O., Huang, Y., Wight, A., Cho, J. W., Zhao, X., Estivill, G., Adam, I., Sanchez, X., McCarthy, S., Schaller, J., Khan, Z., Ruzo, A., Pastorello, R., Richardson, E. T., Dillon, D., Montero-Llopis, P., Barroso-Sousa, R., … Agudo, J. (2022). Quiescent cancer cells resist T cell attack by forming an immunosuppressive niche. *Cell*, *185*(10). https://doi.org/10.1016/j.cell.2022.03.033

12. Turrell, F. K., Orha, R., Guppy, N. J., Gillespie, A., Guelbert, M., Starling, C., Haider, S., & Isacke, C. M. (2023). Age-associated microenvironmental changes highlight the role of PDGF-C in ER+ breast cancer metastatic relapse. *Nature Cancer*, *4*(4). https://doi.org/10.1038/s43018-023-00525-y

13. Wang, J., Ocadiz-Ruiz, R., Hall, M. S., Bushnell, G. G., Orbach, S. M., Decker, J. T., Raghani, R. M., Zhang, Y., Morris, A. H., Jeruss, J. S., & Shea, L. D. (2023). A synthetic metastatic niche reveals antitumor neutrophils drive breast cancer metastatic dormancy in the lungs. *Nature Communications*, *14*(1). https://doi.org/10.1038/s41467-023-40478-5

14. Bushnell, G. G., Sharma, D., Wilmot, H. C., Zheng, M., Fashina, T. D., Hutchens, C. M., Osipov, S., Burness, M., & Wicha, M. S. (2024). Natural Killer Cell Regulation of Breast Cancer Stem Cells Mediates Metastatic Dormancy. *Cancer Research*. https://doi.org/10.1158/0008-5472.can-24-0030

15. Edwards, A., & Brennan, K. (2021). Notch Signalling in Breast Development and Cancer. In *Frontiers in Cell and Developmental Biology* (Vol. 9). https://doi.org/10.3389/fcell.2021.692173

16. Chen, W., Wei, W., Yu, L., Ye, Z., Huang, F., Zhang, L., Hu, S., & Cai, C. (2021). Mammary Development and Breast Cancer: a Notch Perspective. In *Journal of Mammary Gland Biology and Neoplasia* (Vol. 26, Issue 3). https://doi.org/10.1007/s10911-021-09496-1

17. Politi, K., Feirt, N., & Kitajewski, J. (2004). Notch in mammary gland development and breast cancer. *Seminars in Cancer Biology*, *14*(5). https://doi.org/10.1016/j.semcancer.2004.04.013

18. Siebel, C., & Lendahl, U. (2017). Notch signaling in development, tissue homeostasis, and disease. *Physiological Reviews*, *97*(4). https://doi.org/10.1152/physrev.00005.2017

19. Shi, Q., Xue, C., Zeng, Y., Yuan, X., Chu, Q., Jiang, S., Wang, J., Zhang, Y., Zhu, D., & Li, L. (2024). Notch signaling pathway in cancer: from mechanistic insights to targeted therapies. *Signal Transduction and Targeted Therapy*, *9*(1), 128. https://doi.org/10.1038/s41392-024-01828-x

20. Capulli, M., Hristova, D., Valbret, Z., Carys, K., Arjan, R., Maurizi, A., Masedu, F., Cappariello, A., Rucci, N., & Teti, A. (2019). Notch2 pathway mediates breast cancer cellular dormancy and mobilisation in bone and contributes to haematopoietic stem cell mimicry. *British Journal of Cancer*, *121*(2). https://doi.org/10.1038/s41416-019-0501-y

21. Khalil, B. D., Sanchez, R., Rahman, T., Rodriguez-Tirado, C., Moritsch, S., Rodriguez Martinez, A., Miles, B., Farias, E., Mezei, M., Nobre, A. R., Singh, D., Kale, N., Sproll, K. C., Sosa, M. S., & Aguirre-Ghiso, J. A. (2021). An NR2F1-specific agonist suppresses metastasis by inducing cancer cell dormancy. *Journal of Experimental Medicine*, *219*(1). https://doi.org/10.1084/jem.20210836

22. Li, S. Y., Hammarlund, J. A., Wu, G., Lian, J. W., Howell, S. J., Clarke, R. B., Adamson, A. D., Gonçalves, C. F., Hogenesch, J. B., Anafi, R. C., & Meng, Q. J. (2024). Tumor circadian clock strength influences metastatic potential and predicts patient prognosis in luminal A breast cancer. *Proceedings of the National Academy of Sciences of the United States of America*, *121*(7). https://doi.org/10.1073/pnas.2311854121

23. Simões, B. M., O'Brien, C. S., Eyre, R., Silva, A., Yu, L., Sarmiento-Castro, A., Alférez, D. G., Spence, K., Santiago-Gómez, A., Chemi, F., Acar, A., Gandhi, A., Howell, A., Brennan, K., Rydén, L., Catalano, S., Andó, S., Gee, J., Ucar, A., … Clarke, R. B. (2015). Anti-estrogen Resistance in Human Breast Tumors Is Driven by JAG1-NOTCH4-Dependent Cancer Stem Cell Activity. *Cell Reports*, *12*(12). https://doi.org/10.1016/j.celrep.2015.08.050

24. Castella, P., Sawai, S., Nakao, K., Wagner, J. A., & Caudy, M. (2000). HES-1 Repression of Differentiation and Proliferation in PC12 Cells: Role for the Helix 3-Helix 4 Domain in Transcription Repression. *Molecular and Cellular Biology*, *20*(16). https://doi.org/10.1128/mcb.20.16.6170-6183.2000

25. Hartman, J., Müller, P., Foster, J. S., Wimalasena, J., Gustafsson, J. Å., & Ström, A. (2004). HES-1 inhibits 17{$β$}-estradiol and heregulin-{$β$}1-mediated upregulation of E2F-1. *Oncogene*, *23*(54). https://doi.org/10.1038/sj.onc.1208139

26. Murata, K., Hattori, M., Hirai, N., Shinozuka, Y., Hirata, H., Kageyama, R., Sakai, T., & Minato, N. (2005). Hes1 Directly Controls Cell Proliferation through the

Transcriptional Repression of p27 Kip1. *Molecular and Cellular Biology*, *25*(10). https://doi.org/10.1128/mcb.25.10.4262-4271.2005

27. Noda, N., Honma, S., & Ohmiya, Y. (2011). Hes1 is required for contact inhibition of cell proliferation in 3T3-L1 preadipocytes. *Genes to Cells*, *16*(6). https://doi.org/10.1111/j.1365-2443.2011.01518.x

28. Cenciarelli, C., Marei, H. E., Zonfrillo, M., Casalbore, P., Felsani, A., Giannetti, S., Trevisi, G., Althani, A., & Mangiola, A. (2017). The interference of Notch1 target Hes1 affects cell growth, differentiation and invasiveness of glioblastoma stem cells through modulation of multiple oncogenic targets. *Oncotarget*, *8*(11). https://doi.org/10.18632/oncotarget.15013

29. Hartman, J., Lam, E. W. F., Gustafsson, J. Å., & Ström, A. (2009). Hes-6, an inhibitor of Hes-1, is regulated by 17{$β$}-estradiol and promotes breast cancer cell proliferation. *Breast Cancer Research*, *11*(6). https://doi.org/10.1186/bcr2446

30. Shimojo, H., Ohtsuka, T., & Kageyama, R. (2008). Oscillations in Notch Signaling Regulate Maintenance of Neural Progenitors. *Neuron*, *58*(1). https://doi.org/10.1016/j.neuron.2008.02.014

31. Imayoshi, I., Ishidate, F., & Kageyama, R. (2015). Real-time imaging of bHLH transcription factors reveals their dynamic control in the multipotency and fate choice of neural stem cells. In *Frontiers in Cellular Neuroscience* (Vol. 9, Issue AUGUST). https://doi.org/10.3389/fncel.2015.00288

32. Manning, C. S., Biga, V., Boyd, J., Kursawe, J., Ymisson, B., Spiller, D. G., Sanderson, C. M., Galla, T., Rattray, M., & Papalopulu, N. (2019). Quantitative single-cell live imaging links HES5 dynamics with cell-state and fate in murine neurogenesis. *Nature Communications*, *10*(1). https://doi.org/10.1038/s41467-019-10734-8

33. Zhang, Y., Lahmann, I., Baum, K., Shimojo, H., Mourikis, P., Wolf, J., Kageyama, R., & Birchmeier, C. (2021). Oscillations of Delta-like1 regulate the balance between differentiation and maintenance of muscle stem cells. *Nature Communications*, *12*(1). https://doi.org/10.1038/s41467-021-21631-4

34. Miller, A., Biga, V., Rowntree, A., Chhatriwala, M., Woods, F., Noble, B., Marinopoulou, E., Kamath, A., Vallier, L., & Papalopulu, N. (2025). NGN3 oscillatory expression controls the timing of human pancreatic endocrine differentiation. *Developmental Cell*. https://doi.org/10.1016/j.devcel.2025.06.004

35. Sueda, R., Imayoshi, I., Harima, Y., & Kageyama, R. (2019). High Hes1 expression and resultant Ascl1 suppression regulate quiescent vs. active neural stem cells in the adult mouse brain. *Genes and Development*, *33*(9–10). https://doi.org/10.1101/gad.323196.118

36. Maeda, Y., Isomura, A., Masaki, T., & Kageyama, R. (2023). Differential cell-cycle control by oscillatory versus sustained Hes1 expression via p21. *Cell Reports*, *42*(5). https://doi.org/10.1016/j.celrep.2023.112520

37. Marinopoulou, E., Biga, V., Sabherwal, N., Miller, A., Desai, J., Adamson, A. D., & Papalopulu, N. (2021). HES1 protein oscillations are necessary for neural stem cells to exit from quiescence. *IScience*, *24*(10). https://doi.org/10.1016/j.isci.2021.103198

38. Sabherwal, N., Rowntree, A., Marinopoulou, E., Pettini, T., Hourihane, S., Thomas, R., Soto, X., Kursawe, J., & Papalopulu, N. (2021). Differential phase register of Hes1 oscillations with mitoses underlies cell-cycle heterogeneity in ER+ breast cancer cells. *Proceedings of the National Academy of Sciences of the United States of America*, *118*(45). https://doi.org/10.1073/pnas.2113527118

39. Trotter, E. W., & Hagan, I. M. (2020). Release from cell cycle arrest with Cdk4/6 inhibitors generates highly synchronized cell cycle progression in human cell culture: Cdk4/6 Induction Synchronisation. *Open Biology*, *10*(10). https://doi.org/10.1098/rsob.200200rsob200200

40. Crozier, L., Foy, R., Mouery, B. L., Whitaker, R. H., Corno, A., Spanos, C., Ly, T., Gowen Cook, J., & Saurin, A. T. (2022). CDK4/6 inhibitors induce replication stress to cause long-term cell cycle withdrawal. *The EMBO Journal*, *41*(6). https://doi.org/10.15252/embj.2021108599

41. Miller, I., Min, M., Yang, C., Tian, C., Gookin, S., Carter, D., & Spencer, S. L. (2018). Ki67 is a Graded Rather than a Binary Marker of Proliferation versus Quiescence. *Cell Reports*, *24*(5). https://doi.org/10.1016/j.celrep.2018.06.110

42. Zerjatke, T., Gak, I. A., Kirova, D., Fuhrmann, M., Daniel, K., Gonciarz, M., Müller, D., Glauche, I., & Mansfeld, J. (2017). Quantitative Cell Cycle Analysis Based on an Endogenous All-in-One Reporter for Cell Tracking and Classification. *Cell Reports*, *19*(9). https://doi.org/10.1016/j.celrep.2017.05.022

43. Yoshiura, S., Ohtsuka, T., Takenaka, Y., Nagahara, H., Yoshikawa, K., & Kageyama, R. (2007). Ultradian oscillations of Stat, Smad, and Hes1 expression in response to serum. *Proceedings of the National Academy of Sciences of the United States of America*, *104*(27). https://doi.org/10.1073/pnas.0701837104

44. Monk, N. A. M. (2003). Oscillatory Expression of Hes1, p53, and NF-κB Driven by Transcriptional Time Delays. *Current Biology*, *13*(16). https://doi.org/10.1016/S0960-9822(03)00494-9

45. Bonev, B., Stanley, P., & Papalopulu, N. (2012). MicroRNA-9 modulates hes1 ultradian oscillations by forming a double-negative feedback loop. *Cell Reports*, *2*(1). https://doi.org/10.1016/j.celrep.2012.05.017

46. Webb, A. B., Lengyel, I. M., Jörg, D. J., Valentin, G., Jülicher, F., Morelli, L. G., & Oates, A. C. (2016). Persistence, period and precision of autonomous cellular oscillators from the zebrafish segmentation clock. *ELife*, *5*(FEBRUARY2016). https://doi.org/10.7554/eLife.08438

47. Minchington, T. G., Griffiths-Jones, S., & Papalopulu, N. (2020). Dynamical gene regulatory networks are tuned by transcriptional autoregulation with microRNA feedback. *Scientific Reports*, *10*(1). https://doi.org/10.1038/s41598-020-69791-5

48. Soto, X., Biga, V., Kursawe, J., Lea, R., Doostdar, P., Thomas, R., & Papalopulu, N. (2020). Dynamic properties of noise and Her6 levels are optimized by miR-9, allowing the decoding of the Her6 oscillator. *The EMBO Journal*, *39*(12). https://doi.org/10.15252/embj.2019103558

49. Harton, M. D., Koh, W. S., Bunker, A. D., Singh, A., & Batchelor, E. (2019). p53 pulse modulation differentially regulates target gene promoters to regulate cell fate decisions. *Molecular Systems Biology*, *15*(9). https://doi.org/10.15252/msb.20188685

50. Penny, W. D., Duzel, E., Miller, K. J., & Ojemann, J. G. (2008). Testing for nested oscillation. *Journal of Neuroscience Methods*, *174*(1). https://doi.org/10.1016/j.jneumeth.2008.06.035

51. Biga, V., Hawley, J., Soto, X., Johns, E., Han, D., Bennett, H., Adamson, A. D., Kursawe, J., Glendinning, P., Manning, C. S., & Papalopulu, N. (2021). A dynamic, spatially periodic, micro-pattern of HES5 underlies neurogenesis in the mouse spinal cord. *Molecular Systems Biology*, *17*(5). https://doi.org/10.15252/msb.20209902

52. Doostdar, P., Hawley, J., Chopra, K., Marinopoulou, E., Lea, R., Arashvand, K., Biga, V., Papalopulu, N., & Soto, X. (2024). Cell coupling compensates for changes in single-cell Her6 dynamics and provides phenotypic robustness. *Development*, *151*(10). https://doi.org/10.1242/dev.202640

53. Carrieri, F. A., Murray, P. J., Ditsova, D., Ferris, M. A., Davies, P., & Dale, J. K. (2019). CDK1 and CDK2 regulate NICD1 turnover and the periodicity of the segmentation clock. *EMBO Reports*, *20*(7). https://doi.org/10.15252/embr.201846436

54. Hardwick, L. J. A., & Philpott, A. (2019). N-terminal phosphorylation of xHes1 controls inhibition of primary neurogenesis in Xenopus. *Biochemical and Biophysical Research Communications*, *509*(2). https://doi.org/10.1016/j.bbrc.2018.12.135

55. Pack, L. R., Daigh, L. H., Chung, M., & Meyer, T. (2021). Clinical CDK4/6 inhibitors induce selective and immediate dissociation of p21 from cyclin D-CDK4 to inhibit CDK2. *Nature Communications*, *12*(1). https://doi.org/10.1038/s41467-021-23612-z

56. Rowntree, A., Sabherwal, N., & Papalopulu, N. (2022). Bilateral Feedback in Oscillator Model Is Required to Explain the Coupling Dynamics of Hes1 with the Cell Cycle. *Mathematics*, *10*(13), 2323. https://doi.org/10.3390/math10132323

57. Pfeuty, B. (2015). A computational model for the coordination of neural progenitor self-renewal and differentiation through hes1 dynamics. *Development (Cambridge)*, *142*(3). https://doi.org/10.1242/dev.112649

58. Bonev, B., Pisco, A., & Papalopulu, N. (2011). MicroRNA-9 Reveals Regional Diversity of Neural Progenitors along the Anterior-Posterior Axis. *Developmental Cell*, *20*(1). https://doi.org/10.1016/j.devcel.2010.11.018

59. VanderPlas, J. T. (2018). Understanding the Lomb–Scargle Periodogram. *The Astrophysical Journal Supplement Series*, *236*(1). https://doi.org/10.3847/1538-4365/aab766

60. Casini, A., Deng, T., & Perron, P. (2024). Theory of low frequency contamination from nonstationarity and misspecification: consequences for HAR inference. *Econometric Theory*. https://doi.org/10.1017/S026646662400032X

61. Hübner, M., Huppenkothen, D., Lasky, P. D., & Inglis, A. R. (2022). Pitfalls of Periodograms: The Nonstationarity Bias in the Analysis of Quasiperiodic Oscillations. *The Astrophysical Journal Supplement Series*, *259*(2), 32. https://doi.org/10.3847/1538-4365/ac49ec

Figures

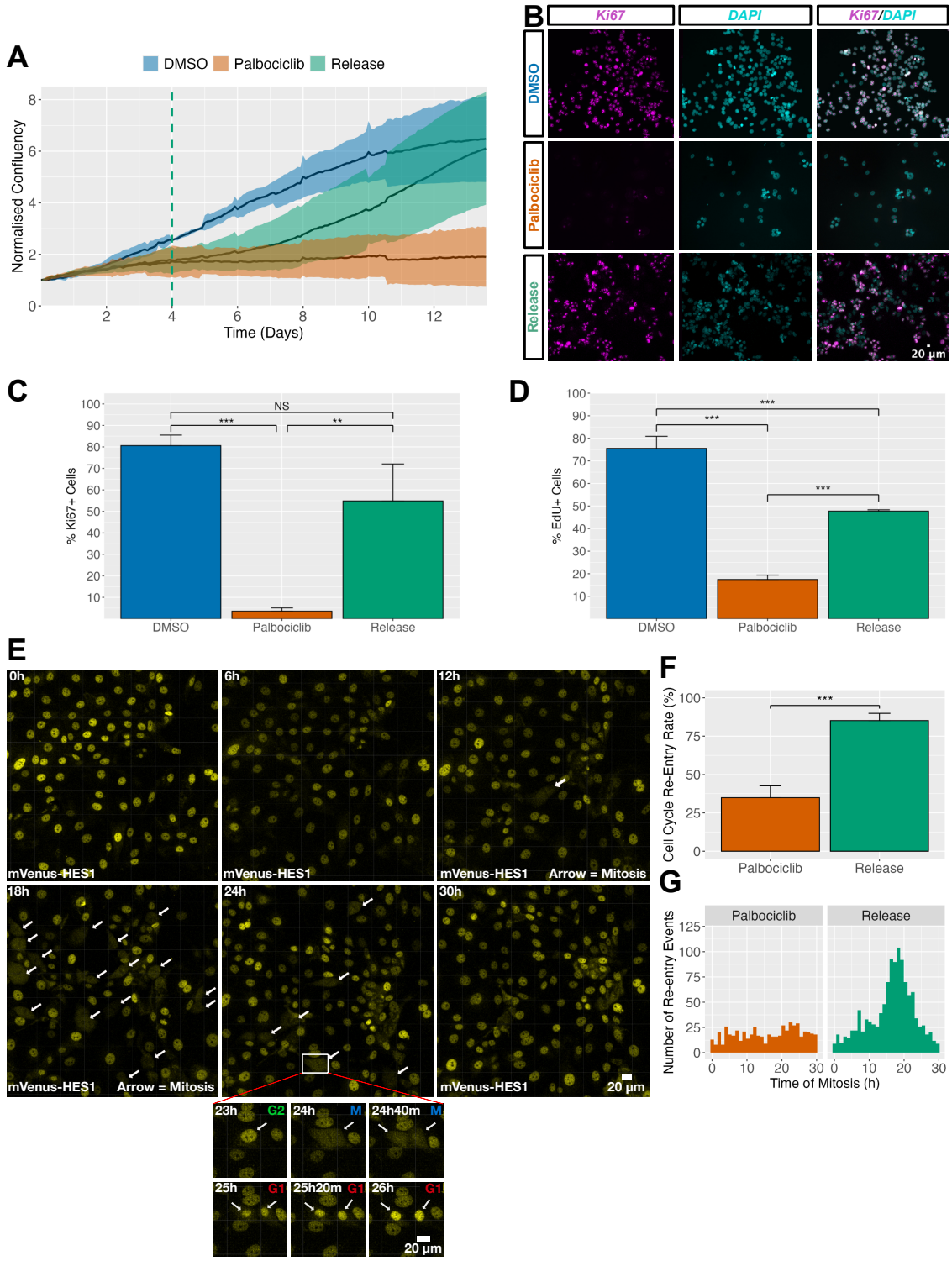

Figure 1. Palbociclib-induced reversible G0/G1 arrest in MCF-7 cells to model ER+ breast cancer dormancy and re-awakening.

(A) Population-level growth curves of MCF-7 cells treated with DMSO (proliferative control), continuous palbociclib, or palbociclib followed by release into proliferative media after 4

days. Lines represent the mean of *N* = 4 biological replicates; shaded areas show standard deviation (SD). Confluency was normalised to baseline values at the start of the time course.

(B) Representative immunofluorescence images of cells from each condition stained for the proliferation marker Ki67. Cells were released from palbociclib after 3 days herein.

(C) Automated quantification of Ki67^{+} cells from (B). Bars represent mean ± SD from *N* = 3 biological replicates, with *n* = 1,371 (DMSO), 1,135 (palbociclib), and 1,082 (release) cells analysed. Statistical significance was assessed by independent *t*-test: ***$p < 0.001$, **$p < 0.01$.

(D) Fraction of EdU+ cells after a 24h pulse, measured by flow cytometry. Bars represent mean ± SD from *N* = 3 biological replicates with *n* = 11,929 (DMSO), 9,014 (palbociclib), and 10,626 (release) cells analysed. Independent *t*-test: ***$p < 0.001$.

(E) Representative time-lapse snapshots from single-cell live imaging of MCF-7 cells released from palbociclib arrest. Imaging commenced ~1h post-release. Endogenous mVenus-HES1 signal was used as a nuclear marker. White arrows indicate cells undergoing mitosis. Inset demonstrates a cell entering mitosis and undergoing division.

(F) Percentage of cells in (E) undergoing mitosis within 30h post-release, defined as 're-entry' events. Bars show mean ± SD from *N* = 3 replicates with *n* = 560 (palbociclib) and 1,162 (release) cells analysed. Independent *t*-test: ***$p < 0.001$.

(G) Histogram showing the timing of re-entry events in (E), pooled across single cells from *N* = 3 replicates.

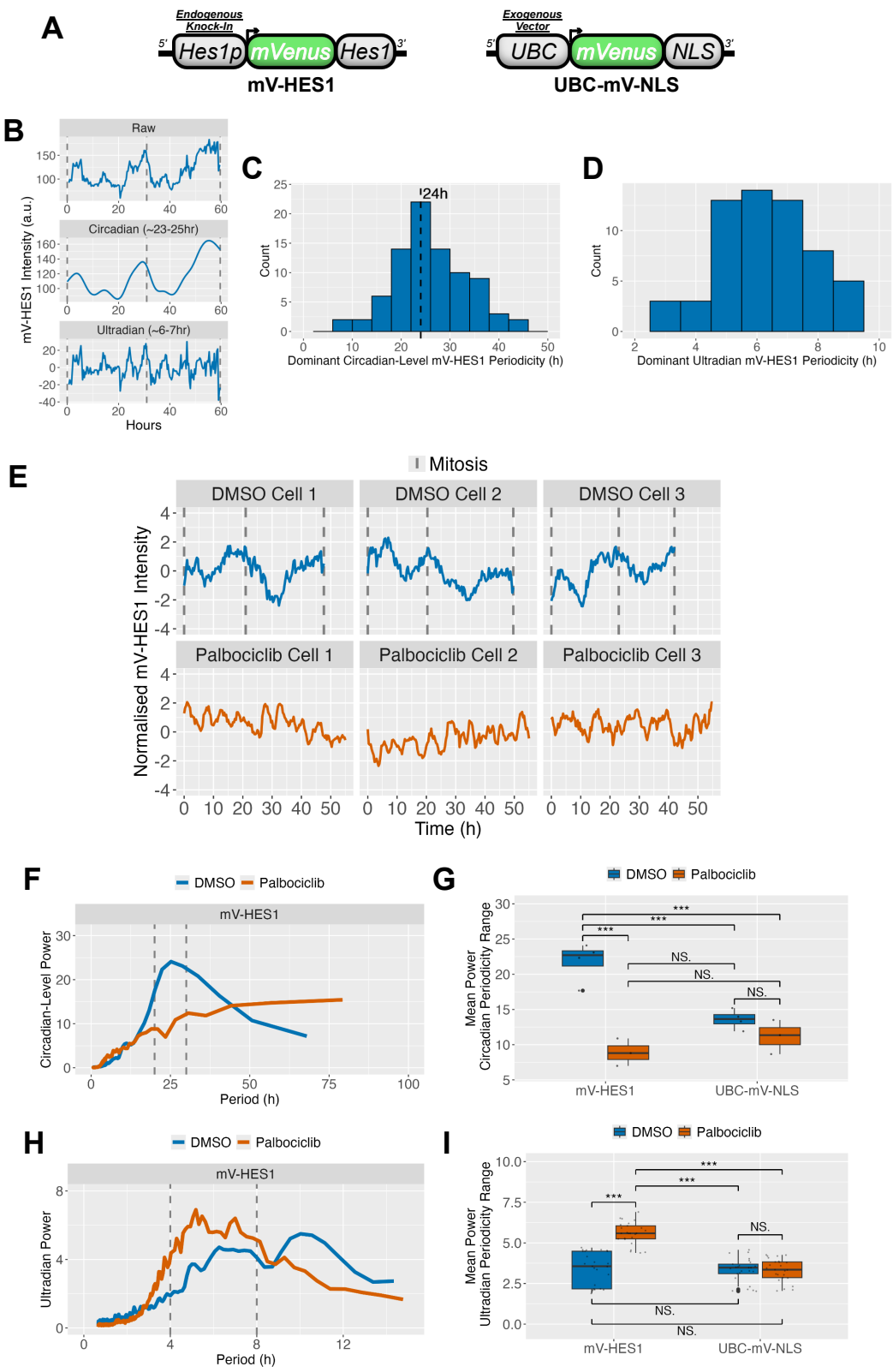

Figure 2. Circadian-level HES1 oscillations are absent during arrest, while ultradian periodicity is enhanced.

(A) Schematic diagram of the endogenous mVenus-HES1 fusion reporter knocked-in at the endogenous HES1 locus in MCF-7 cells via CRISPR (left), alongside control exogenous UBC-mVenus-NLS introduced by lentiviral transduction (right).

(B) Representative single-cell time-series of mVenus fluorescence intensity from a proliferative mV-HES1 cell. Raw signal (top) is shown alongside detrended signals isolating circadian-level (middle) and ultradian (bottom) oscillations from the same cell. Vertical grey lines mark mitosis events.

(C, D) Histogram to show estimated circadian-level (C) and ultradian (D) periodicities in proliferative mV-HES1 cells derived from Lomb-Scargle periodogram (LSP) approach. N = 3 independent experiments *;* n = 90 cells.

(E) Representative Z-score normalized time-series of mV-HES1 cells continuously live-imaged in proliferative (DMSO control) or arrested (palbociclib) conditions. Grey lines indicate mitoses.

(F) Mean normalised LSP power spectra of detrended time-series data from (E), highlighting the relative strength of oscillations across a range of periodicities. Grey lines indicate circadian frequency range used for analysis in (G). N = 3 independent experiments; n = 90 cells per group.

(G) Comparison of oscillation power within the circadian frequency range (20-30h) between mV-HES1 and UBC-mVenus-NLS cells ± palbociclib, based on data in (F). Each point represents mean power at a given circadian-level frequency averaged across all cells and replicates. Statistical significance assessed by ANOVA with Tukey's post-hoc test; all significant comparisons shown. ***$p < 0.001$.

(H, I) As in (F) and (G), but for ultradian oscillations (4-8h range) using appropriately detrended time-series.

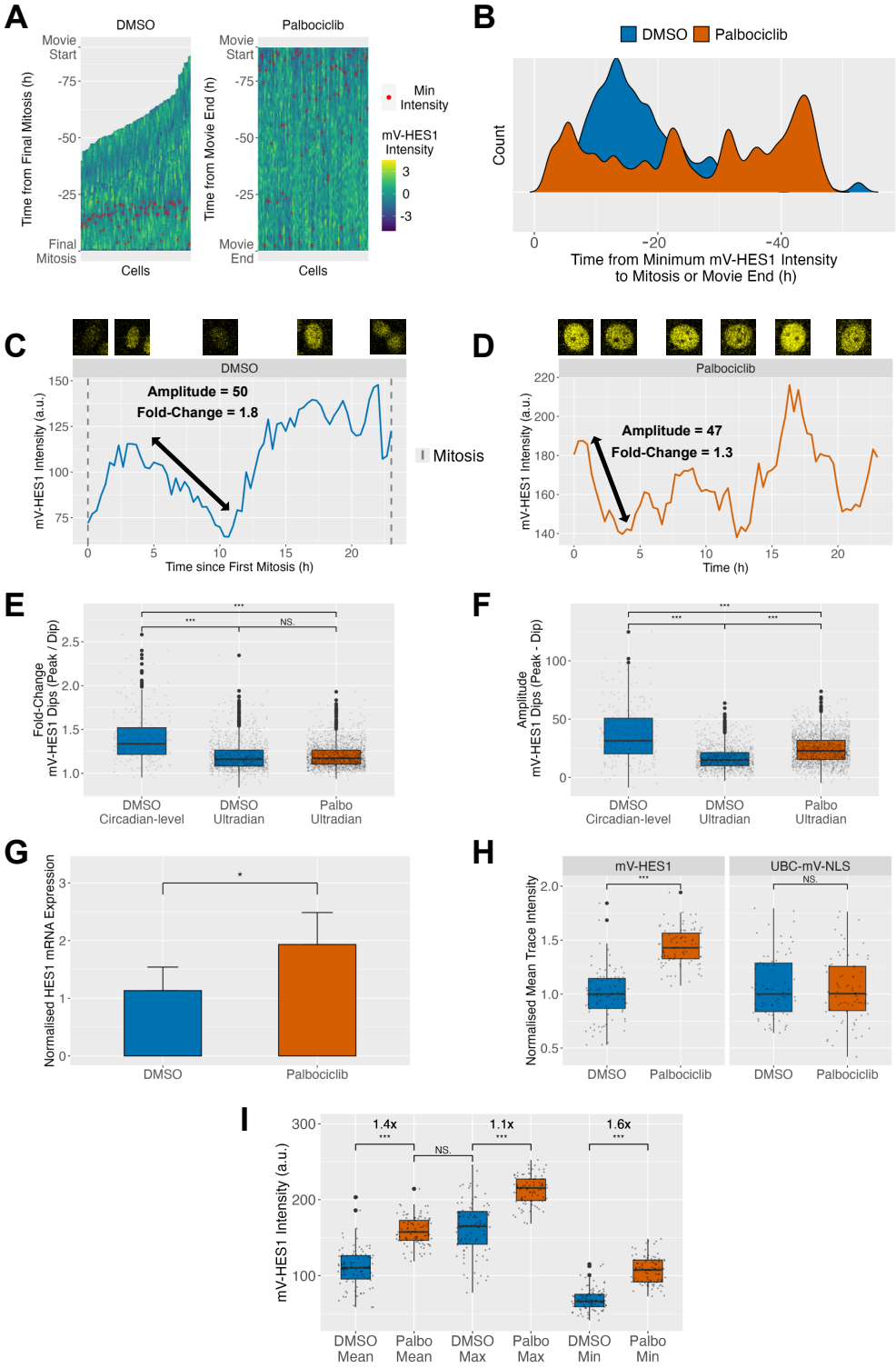

Figure 3. HES1 is maintained at a higher level and exhibits smaller dips during arrest.

(A) Z-score normalised mV-HES1 time-series from cells in proliferative (DMSO) or arrested (palbociclib) conditions plotted as heatmaps. Each x-axis point represents a distinct cell; each trace includes two consecutive cell cycle generations with three mitoses. DMSO traces are aligned (T = 0 h) to the final mitosis, while palbociclib traces are aligned to the end of the movie. Tile brightness reflects normalised signal intensity. Red dots indicate the time of minimum mV-HES1 intensity in the daughter generation (DMSO – G1/S HES1 dip) or full trace (palbociclib). *N* = 3 experiments, *n* = 90 cells per condition.

(B) Histogram density plot showing the timing of minimum mV-HES1 intensity from (A). T = 0 h denotes final mitosis (DMSO) or end of movie (palbociclib).

(C, D) Representative raw mV-HES1 single-cell time-series from DMSO (C) or palbociclib (D) conditions, with overlaid nuclear images corresponding to the mV-HES1 trace. Amplitude and fold-change of the first peak-dip pair are annotated. Grey lines mark mitoses.

(E, F) Fold-change (E) and amplitude (F) for each peak–dip pair in mV-HES1 traces. Data compared across DMSO traces detrended for circadian-level periodicity, DMSO traces detrended for ultradian periodicity, and palbociclib traces detrended for ultradian periodicity. *N* = 3 experiments, *n* = 90 cells per condition. Statistical analysis via ANOVA with Tukey's post-hoc test. ***$p < 0.001$.

(G) mV-HES1 cells were treated with 1 µM palbociclib for 3 days before HES1 mRNA levels were measured by RT-qPCR. Bars show mean ± SD from *N* = 6 experiments. Independent t-test: *$p < 0.05$.

(H) Mean mVenus fluorescence intensity per cell was calculated from raw time-series and normalised to the median DMSO value for each cell line (mV-HES1 or control UBC-mV-NLS). *N* = 3 experiments, *n* = 90 cells per condition. Independent t-test: ***$p < 0.001$.

(I) As in (H), showing mean, maximum, and minimum intensity per mV-HES1 cells ± palbociclib. Annotated old-changes represent the ratio between DMSO and palbociclib median values. *N* = 3 experiments, *n* = 90 cells per condition. Independent t-test: ***$p < 0.001$.

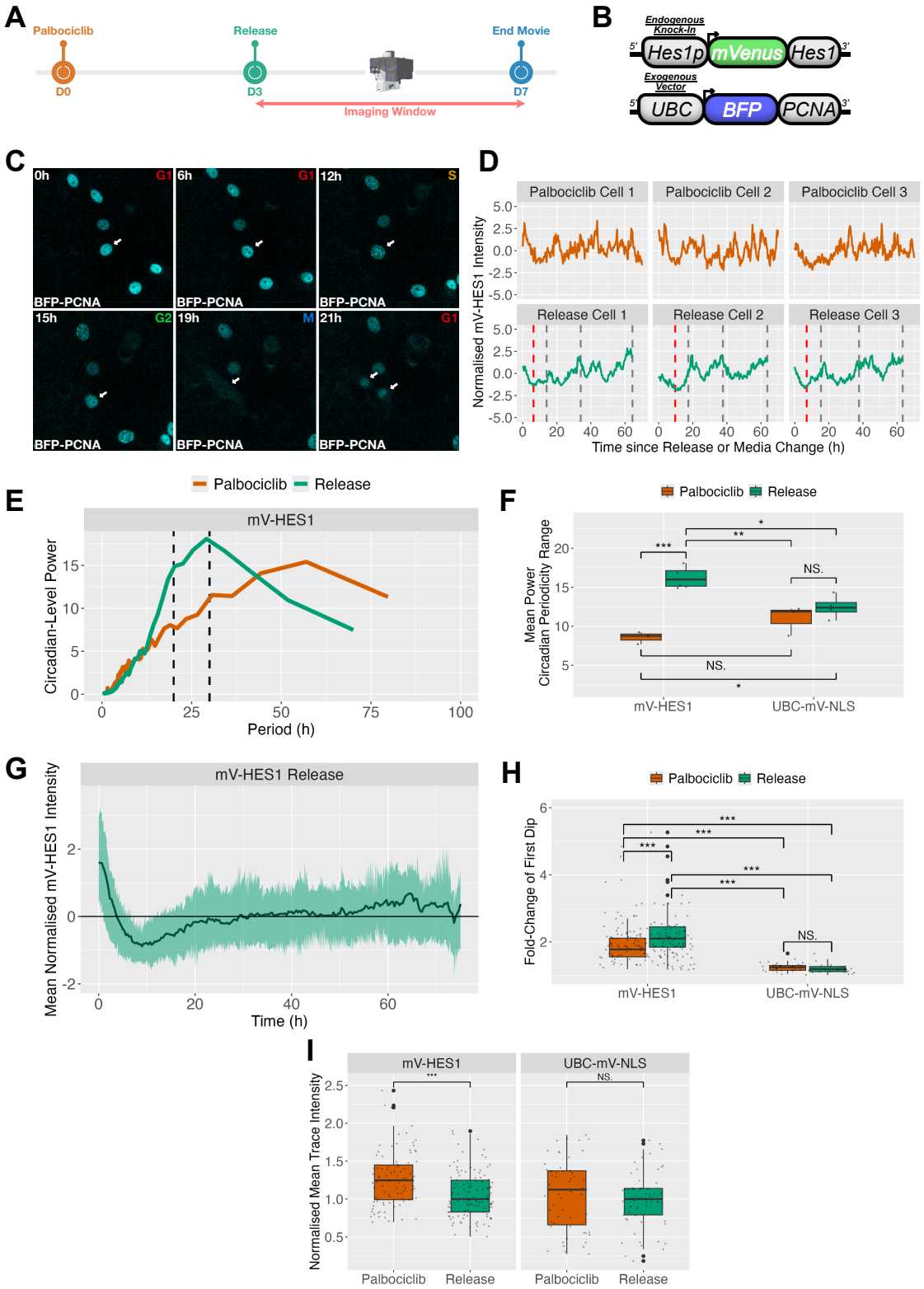

Figure 4. HES1 circadian-level oscillations resume and G1/S dip is observed upon cell cycle re-entry.

(A) Schematic of the experimental timeline: cells were arrested with palbociclib for 3 days, then released into proliferative media and monitored by continuous live imaging for an additional 4 days.

(B) Schematic of constructs present in the cells. The UBC-BFP-PCNA cell cycle reporter was introduced into mV-HES1 cells to mark S-phase entry via a punctate nuclear pattern.

(C) Representative snapshots from single-cell live imaging of mV-HES1 UBC-BFP-PCNA cells. The white arrow highlights a single cell progressing through the cell cycle. Cell cycle stages, inferred from PCNA pattern, are indicated in the top right corner. The punctate pattern visible at 12 h marks S-phase.

(D) Representative mV-HES1 single-cell time-series following palbociclib release (release) or maintained arrest (palbociclib). For release cells, time is relative to palbociclib withdrawal; for arrested cells, time is relative to a media change with fresh palbociclib. mV-HES1 fluorescence intensity was Z-score normalised. Grey lines indicate mitoses; red lines mark S-phase in the first generation after release.

(E) LSP power spectra of circadian-detrended traces from (D). Spectra represent the mean of single-cell traces from each group. Lines indicate frequencies corresponding to the indicated periods. N = 3 experiments; n = 115 (Release), 90 (Palbociclib) cells.

(F) Comparison of mean LSP power within the circadian frequency range (20–30 h) for released vs. arrested cells expressing either mV-HES1 or control UBC-mV-NLS. Each data point represents mean power at a given circadian-level frequency across all cells and replicates. N = 3 experiments; n = 55–115 cells per group. ANOVA with Tukey's post-hoc test; all significant comparisons shown.***$p < 0.001$, **$p < 0.01$, *$p < 0.05$.

(G) Mean Z-score normalised mV-HES1 trace from released cells illustrating the prominent dip following release. Line indicates the mean of n = 115 cells pooled from N = 3 experiments; shading indicates SD.

(H) Fold-change was calculated between mVenus intensity at release and the minimum intensity prior to the 1st mitosis (release cells) or within the first 15h (palbociclib cells), for both mV-HES1 and UBC-mV-NLS cells. N = 3 experiments; n = 55–115 cells per group. Independent t-test: ***$p < 0.001$.

(I) Mean mVenus fluorescence intensity per cell was calculated from raw time-series and normalised to the median value from released cells for each cell line (mV-HES1 or control UBC-mV-NLS). N = 3 experiments, n = 55-115 cells per condition. Independent t-test *** < 0.001.

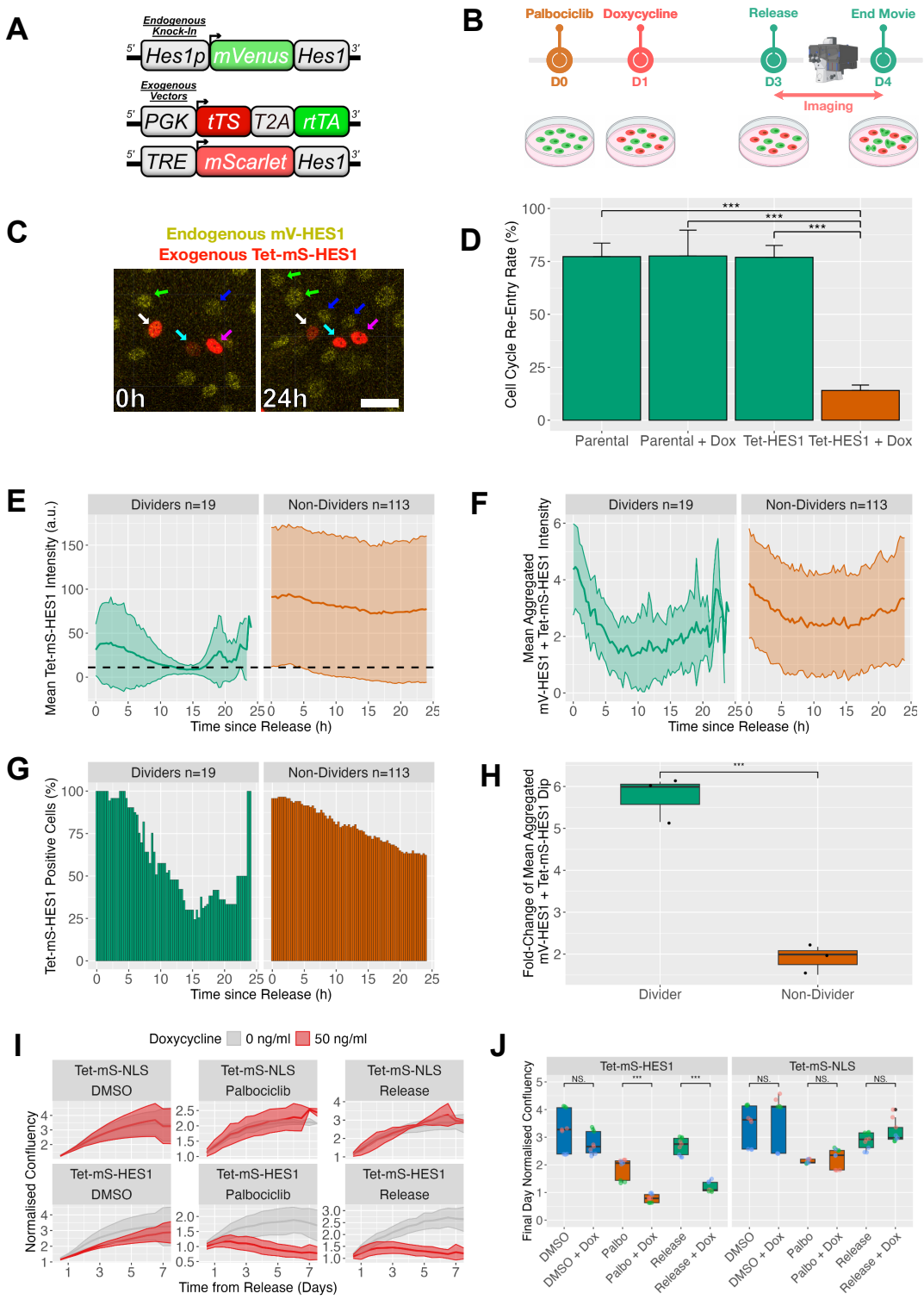

Figure 5. Sustained expression of HES1 during release from palbociclib impedes cell cycle re-entry.

(A) Schematic of constructs present in cells. Tet-On lentiviral vectors were incorporated into mV-HES1 cells to enable doxycycline-inducible Tet-mS-HES1 expression.

(B) Schematic of the 24h release assay used in (C-H). Cells were arrested with palbociclib for 3 days, then released into proliferative media ± doxycycline. Continuous live imaging was

performed post-release for 24h to assess cell cycle re-entry. Cartoon illustrates a typical field: red and green nuclei indicate cells that did or did not turn on Tet-mS-HES1, respectively.

(C) Representative time-lapse images from the 24h release assay. Images show cells at 0h (release) and 24h. Arrow colours mark distinct cell lineages. Highlighted cells without induced Tet-mS-HES1 expression divided during the time course (green and blue arrows), whereas cells with sustained HES1 expression did not divide (white, cyan, magenta arrows), indicating a block in re-entry. Scale bar = 40 µm.

(D) Quantification of the proportion of cells that underwent mitosis (re-entered the cell cycle) during the 24h release assay. Parental and Tet-HES1 refer to mV-HES1 cells with or without Tet constructs to express Tet-mS-HES1, respectively. Doxycycline was used at 5 ng/mL. Cells that died during imaging were excluded. Bars show the mean proportion from $N = 3$ experiments; $n = 130–180$ cells per group. Error bars indicate SD. Independent t-test: ***$p < 0.001$.

(E) Single-cell time-series of Tet-mS-HES1 expression from doxycycline-treated Tet-HES1 cells in the 24h release assay (D). Traces were grouped by division fate (Dividers vs. Non-Dividers) and averaged. The positivity threshold for Tet-mS-HES1 expression is indicated (black horizontal line).

(F) As in (E), but combining exogenous Tet-mS-HES1 and endogenous mV-HES1 signals to visualise total HES1 protein per cell. Signals were Z-score normalised before combination.

(G) Cells were classified as Tet-mS-HES1 positive or negative at each timepoint using the threshold from (E). The percentage of positive cells was plotted over time for Dividers (left) and Non-Dividers (right).

(H) Fold-change in total HES1 expression (from release to minimum intensity) was calculated using the combined mean traces in (F). Each dot represents one experiment. Independent t-test: ***$p < 0.001$.

(I) Seven-day release assay showing population growth curves post-release. mV-HES1 cells expressing Tet-mS-HES1 or a control Tet-mS-NLS reporter were monitored in proliferative (DMSO), arrested (palbociclib), or released conditions ± doxycycline (50 ng/mL). Lines indicate mean confluency normalised to initial confluency; shading shows SD. $N = 3$ experiments.

(J) Quantification of the 7-day growth curves from (I). Confluency measurements from the final day (3 time-points per day per experiment) were pooled and compared across conditions. ANOVA with Tukey's post-hoc test: ***$p < 0.001$